

2-3-2 A 3-D MHD Simulation Model of the Solar Corona-Solar Wind System

NAKAMIZO Aoi, KUBO Yūki, and TANAKA Takashi

In the framework of integrated numerical space weather prediction, we have developed a 3-D MHD simulation model of the solar surface-solar wind system. We report the construction method of the model and its first results. By implementing a grid system with angularly unstructured and increasing radial spacing, we realized a spherical grid that have no pole singularity and realized a fine grid size around the inner boundary and a wide-range grid up to a size of 1 AU simultaneously. The magnetic field at the inner boundary is specified by the observational data. In order to obtain the supersonic solar wind speed, parameterized source functions are introduced into the momentum and energy equations. The simulation simultaneously reproduces the plasma-exit structure, the high- and low-temperature regions, the open and closed magnetic field regions in the corona, the fast and slow solar wind, and the sector structure in interplanetary space. It is confirmed from the comparison with observations that the MHD model successfully reproduces many features of both the fine solar coronal structure and the global solar wind structure. With the further improvement and refinement, the model will be applied to the integrated space weather simulation system being developed in NICT.

Keywords

Solar wind, MHD simulation, Expansion factor

1 Introduction

This work aims at reproducing the heliospheric structure from the solar surface to terrestrial orbit, in order to predict solar winds arriving at the earth as one factor of space weather phenomena.

The basic conceptualization of solar winds dates back to Parker's theory[1]. While the presence of solar winds has been confirmed as an observed fact for about half a century, the originating flow of supersonic plasma from the sun that occupies interplanetary space free from solar gravitation is now being universally recognized. The study of solar winds takes two strikingly opposite approaches. One focuses on the physical process of solar winds as stellar winds. The other concerns the global structures of solar winds and interplanetary space from the per-

spective of the space weather environment. Our work takes the latter approach. First, the physical issues of stellar winds—coronal heating and the mechanism for solar wind acceleration—are classic problems yet to be solved. The observed facts and probes into the elementary process have resulted in numerous theoretical proposals (see [2]–[7]), but no consensus has yet to be reached. Since the beginning of the fully fledged space age in the 1960s, the global structures of solar winds and interplanetary space remain key subjects of present-day exploration. Given the many discoveries since then, including a 27-day periodicity[8] detected by *Mariner 2*, bipolar structures[9][10] by *Ulysses*, and empirical model presentations regarding a source surface model[11][12] and the Wang-Sheeley model[13] that build on these observations, a consensus has been reached to some

extent on the genesis of solar winds during periods of the solar maximum and minimum (see [14][15]). Solar wind predictions now being made by ISEE (International Space Environment Service)-related agencies, and are essentially based on the Wang-Sheeley model or by expanding on the source surface model, though these models are available in various derived versions[16][17].

Solar wind predictions that meet the practical needs of a space weather simulator remain difficult to achieve, however, when based simply on an extension of the solar wind studies cited above. The source surface model is designed to establish the heliosphere relative to the magnetic field structure of the solar neighborhood alone, and does not deal with the physical processes of the solar neighborhood region, which is of vital importance to solar wind acceleration. Elementary process studies, on the other hand, may offer a solution to the acceleration mechanism or variations in velocity, but fall short of presenting the global structure of the heliosphere. Solar winds observed in terrestrial orbit only offer a brief glance at the heliospheric 3D structure, but its genesis originates from the solar neighborhood region. Predicting solar winds in terrestrial orbit therefore requires the solar-heliospheric structure as a whole to be conceived by simultaneously handling the fine structures of the solar neighborhood and the far-reaching global structures covering as wide as 1 AU. With these discussions in mind, we are building a heliospheric global model by using MHD simulations. This paper presents introductory information about development of the model thus far, and reports the initial usage results.

2 Model

This chapter provides summary information about the simulation model.

2.1 Computational grid

Extremely complex solar magnetic fields existing within 2 Rs (Rs = solar radius) of the

solar disk must be calculated with high spatial resolutions. And a region as broad as 1 AU (1 AU = 220 Rs) must also be calculated to predict solar winds in terrestrial orbit. To fulfill both needs, a 2D unstructured grid based on the regular dodecahedron splitting method has been developed. Figure 1 shows the process of grid formation. First, a regular pentagon on each side of a regular dodecahedron (shown in Fig. 1(a)) is split into five triangles (initial splitting) as shown in Fig. 1(b). Next, the middle point on each side of a triangle thus formed is interconnected to split the triangle into four smaller triangles (second-order splitting) as shown in Fig. 1(c). The new vertex formed for each cycle of the procedure is projected on the circumscribing sphere of the original regular dodecahedron. This procedure can be iterated infinitely in principle. Figs. 1 (d), (e) and (f) respectively show the second-, third-, and fifth-order split grids thus formed. Unstructured grids having a spherical surface uniformly covered by triangles of the same size are useful for suppressing numerical instability, because such grids entail neither latitude or longitude dependence nor singular points.

3D grids are formed by stacking 2D unstructured grids (as described above) in the radial direction. Such 3D grids are generally useful for calculating large-scale structures such as those of the solar wind-planetary sys-

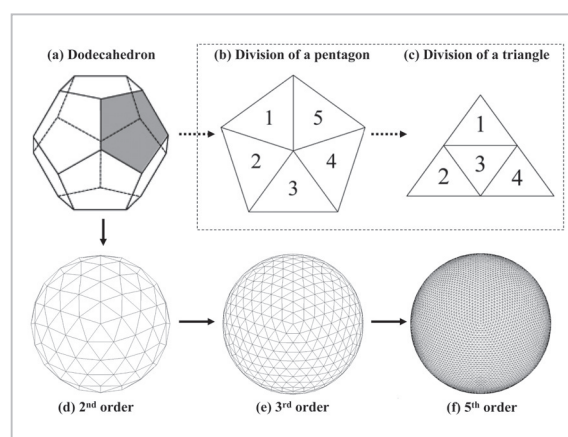


Fig. 1 2D unstructured grid formation

(a) Regular dodecahedron, (b) first-order splitting, (c) second-order splitting, (d), (e), (f) second-, third- and fifth-order split grids

tem and solar-solar wind system that contain fine internal structures. In calculating the structures of the solar-solar wind system, a solar surface is defined in the innermost shell, and with the outermost shell being expanded to a required region. In this paper, the outermost shell was set at 200 Rs in a fifth-order grid (of 7,682 spherical grid points, 115,360 spherical triangles, and spatial resolution in the latitude and longitude directions of about 2.25 degrees), with the spatial resolution in the radial direction having been gradually increased from 0.02 Rs in the innermost part to 2.75 Rs in the outermost part.

2.2 Equation system

The system of equations for evolution of the solar-solar wind system is based on modified MHD equations[18] as shown below, with magnetic field \mathbf{B} split into potential field \mathbf{B}_0 and deviation component \mathbf{B}_1 .

$$\frac{\partial \rho}{\partial t} + \nabla \cdot (\rho \mathbf{V}) = 0 \quad (1)$$

$$\begin{aligned} \frac{\partial (\rho \mathbf{V})}{\partial t} + \nabla \cdot \left(\rho \mathbf{V} \mathbf{V} + p \mathbf{I} + \frac{B^2 - B_0^2}{2\mu_0} \mathbf{I} - \frac{\mathbf{B}\mathbf{B} - \mathbf{B}_0 \mathbf{B}_0}{\mu_0} \right) \\ = -\rho \frac{GM_s}{r^2} \hat{\mathbf{r}} - 2\rho \boldsymbol{\Omega} \times \mathbf{r} - \rho \boldsymbol{\Omega} \times (\boldsymbol{\Omega} \times \mathbf{r}) + S_M \end{aligned} \quad (2)$$

$$\frac{\partial \mathbf{B}_1}{\partial t} + \nabla \times (\mathbf{V} \times \mathbf{B}) = 0 \quad (3)$$

$$\begin{aligned} \frac{\partial U_1}{\partial t} + \nabla \cdot \left[\mathbf{V} \cdot \left(U_1 + p + \frac{B^2}{2\mu_0} \right) - \frac{\mathbf{B}_1(\mathbf{V} \cdot \mathbf{B}_1)}{\mu_0} - \frac{\mathbf{B}_0(\mathbf{V} \cdot \mathbf{B}_1)}{\mu_0} + \frac{\mathbf{V}(\mathbf{B}_1 \cdot \mathbf{B}_0)}{\mu_0} \right] \\ = \rho \mathbf{V} \cdot \left(-\frac{GM_s}{r^2} \hat{\mathbf{r}} \right) - \rho \mathbf{V} \cdot [\boldsymbol{\Omega} \times (\boldsymbol{\Omega} \times \mathbf{r})] + S_E \end{aligned} \quad (4)$$

$$U_1 = \frac{\rho v^2}{2} + \frac{p}{\gamma - 1} + \frac{B^2}{2\mu_0} \quad (5)$$

where, ρ , \mathbf{V} , and p denote the mass density, fluid velocity, and plasma pressure, respectively. \mathbf{B} , \mathbf{B}_0 , and \mathbf{B}_1 denote the magnetic field, potential field, and deviation component ($\mathbf{B} = \mathbf{B}_0 + \mathbf{B}_1$) from the potential field, respectively. U_1 is the modified total energy density composed of the kinetic energy density, thermal energy density, and magnetic energy density defined by \mathbf{B}_1 . In addition, t denotes the time, \mathbf{r} the position vector from the solar center, $\hat{\mathbf{r}}$ the unit vector of \mathbf{r} , μ_0 the permeability in the vacuum, G the gravitational constant, M_s

the solar mass, $\boldsymbol{\Omega}$ the angular velocity of solar rotation, and γ the specific heat ($= 1 + 2/f$, where f denotes the degree of freedom of the plasma particles). Equations (1), (2), (3) and (4) correspond to the mass conservation, momentum conservation, the induction equation, and energy conservation in the regular MHD equation, respectively. The last terms on the right sides of Equation (2) and Equation (4) denote a momentum source and an energy source, respectively. These external source terms are required for solar wind acceleration as detailed in Section 2.5.

Because the evolution of solar wind is calculated on a system that revolves with the sun, the effects of solar rotation and solar gravitation are factored into the momentum and energy equations. The second and third terms on the right side of Equation (2) represent work done by the Coriolis force and centrifugal force, respectively; the second term on the right side of Equation (4) represents work done by centrifugal force. These apparent effects of rotation are removed when analyzing the calculation results, because the simulation data is converted to a coordinate system at rest.

2.3 Computation scheme

The finite volume method (FVM) developed as explained in Reference[18] is used to facilitate time evolution of the system of MHD equations presented above. Numerical fluxes are converted upstream on the basis of eigenvalue decomposition[19] using a TVD scheme and MUSCL interpolation (using the van Leer limiter). (For details, refer to Reference[18]). Figure 2 shows how a control volume required by the finite volume method is defined on a triangular grid system. Each fine continuous line denotes a grid on a spherical surface (Z_i, Z_{i+1}), and each fine dashed line indicates the continuous line projected on surface $Z_{i+1/2}$ defined between Z_i and Z_{i+1} . The circumcenters of triangles adjoining the grid are connected to define a control volume (i.e., hexagonal column represented by bold continuous lines). Changes in physical quantity at the grid points are calculated from the sum of

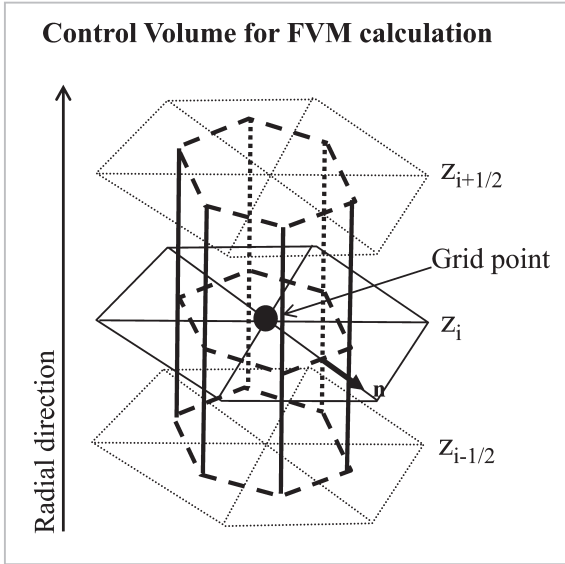


Fig.2 Control volume for the finite volume method

Each fine continuous line denotes a grid on a spherical surface (Z_i, Z_{i+1}), and each fine dashed line indicates the continuous line projected on surface $Z_{i+1/2}$ defined between Z_i and Z_{i+1} . The control volume is a hexagonal column (represented by bold continuous lines) defined by connecting the circumcenters of triangles adjoining the grid.

numerical fluxes entering and leaving the control volume.

2.4 Boundary conditions and initial conditions

Boundary conditions and initial conditions must be set in order to conduct a numeric simulation. Table 1 summarizes the boundary conditions for this model. $V_{||}$ denotes the magnetic field direction component of \mathbf{V} , $V_{\perp,1}$ and $V_{\perp,2}$ the magnetic field vertical components of \mathbf{V} , $B_{1,r}$ the radial direction component of \mathbf{B}_1 , $B_{1,t1}$ and $B_{1,t2}$ the residual components of \mathbf{B}_1 (tangential to the spherical surface), $B_{0,LOS}$ the line-of-sight (LOS) component of \mathbf{B}_0 , and $B_{0,1}$ and $B_{0,2}$ the residual components of \mathbf{B}_0 . (The following describes why \mathbf{B}_0 is decomposed this way. On the external boundary, the Dirichlet conditions are imposed only on U_1 (defined asymptotically for plasma pressure approach 0), with other variables being solved under Neumann conditions. While $V_{||}$, $B_{1,t1}$ and $B_{1,t2}$ are subjected to the Neumann conditions

Table 1 Boundary conditions for MHD simulation

	Inner Boundary 1 Rs	Outer Boundary 200 Rs
ρ (mass density)	fix	$\partial / \partial r=0$
$V_{ }$ (parallel to \mathbf{B})	$\partial / \partial r=0$	$\partial / \partial r=0$
$V_{\perp,1}$ (perpendicular to \mathbf{B})	0	$\partial / \partial r=0$
$V_{\perp,2}$ (perpendicular to \mathbf{B})	0	$\partial / \partial r=0$
\mathbf{B}_1 (perturbed component)	$B_{1,r}$ (radial component)	0
	$B_{1,t1}$ (residual of \mathbf{B}_1)	$\partial / \partial r=0$
	$B_{1,t2}$ (residual of \mathbf{B}_1)	$\partial / \partial r=0$
U_1 (modified total energy density)	fix	fix ($p \rightarrow 0$)
\mathbf{B}_0 (potential magnetic field)	$B_{0,LOS}$ (Line-Of-Site component)	fix (observation)
	$B_{0,1}$ (residual of \mathbf{B}_0)	free
	$B_{0,2}$ (residual of \mathbf{B}_0)	free

on the internal boundary, ρ , $V_{\perp,1}$, $V_{\perp,2}$, $B_{1,r}$ and U_1 are solved under the Dirichlet conditions. The line-of-sight photospheric magnetic field data available from the Wilcox Solar Observatory (<http://wso.stanford.edu/>) is used as $B_{0,LOS}$ to reproduce a realistic solar-solar wind structure. In addition, $B_{1,r}$, $V_{\perp,1}$ and $V_{\perp,2}$ are fixed to maintain constant magnetic flux, with ρ being fixed at $1.5 \times 10^{-13} \text{ kg.m}^{-3}$ (number density of $0.9 \times 10^{14} \text{ m}^{-3}$). U_1 is automatically determined by normalized temperature $T_0 = 0.5 \times 10^6 \text{ K}$. As for the initial conditions, ρ and p both represent a hydrostatic equilibrium, and \mathbf{B} is a potential field with $\mathbf{V} = 0$. The potential field is determined by the conjugate residual method (CR). Under these boundary and initial conditions, the system of MHD equations is subjected to time evolution until reaching a steady state. Here, the steady solution is viewed as a basic structure of solar winds for the period corresponding to observation data $B_{0,LOS}$. Hence, the time phenomenon, such as the formation and propagation of CME, can be left out of the scope of the present work.

2.5 Solar wind acceleration under a solar magnetic field

External terms are factored into the momentum and energy equations for realistic solar wind acceleration. The energy source term is composed of a heating term (first term) and a Spitzer thermal conductivity term (second term).

$$S_E = Q \exp(-R/L_Q) + \nabla \cdot \left(\zeta T^{2.5} \frac{\nabla T \cdot \mathbf{B}}{B^2} \right) \cdot \mathbf{B} \quad (6)$$

where, R denotes distance from the solar center normalized by the solar radius, Q and LQ the strength and decay length of heating, and T the temperature. (This model does not include the thermal conductivity of collisionless plasma.) Though heating terms of this type have been commonly used in past studies (see [21]–[23]) since being first introduced in Reference [20], we took a new approach: heating strength Q is made dependent on magnetic field expansion factor f_s .

$$Q = Q_0 \cdot \frac{1}{f_s}, \quad (7)$$

where, Q_0 denotes a constant and f_s is defined as follows:

$$f_s = \left(\frac{R_s}{R} \right)^2 \frac{B_{R_s}}{B_R}, \quad (8)$$

where, B_{R_s} denotes magnetic field strength on the solar surface. Its dependence on f_s is based on an inverse proportional relation between solar wind velocity and f_s [13][24]. Consequently, the heating term decreases in a region where the magnetic field expands very radially in particular, and increases where the magnetic field expands not so radially. With this method, heating strength distributions better reflect the magnetic field configuration of a region considered important to the generation of solar winds than uniform distributions or simple latitude-dependent distributions.

Note that momentum source term S_M is a function form similar to the heating term.

$$S_M = M(R - 1.0) \exp(-R/L_M), \quad (9)$$

where, M and L_M denote the momentum and attenuation length, respectively. Likewise, M is made dependent on f_s .

$$M = M_0 \cdot \frac{1}{f_s}, \quad (10)$$

where, M_0 denotes a constant. In this paper, Q_0 and M_0 are set to $3.3 \times 10^{-6} \text{ Jm}^{-3\text{s}^{-1}}$ and $5.3 \times 10^{-14} \text{ Nm}^{-3}$, respectively, and L_Q and L_M are set to 0.9 R_s .

3 Simulation results

This chapter introduces the calculation results for the 2028 period of Carrington Rotation (CR) (March 24 to April 21, 2005). Simulation data was first compared with actual observation data regarding the detailed structure of solar coronas, followed by large-scale solar wind structures and interplanetary space for evaluating the model. It would be better to compare model data with observation data during a period of intense solar activity with relatively complex solar magnetic fields than during the solar minimum when solar coronas and solar winds have extremely simple structures. Establishing a one-to-one correspondence between solar magnetic fields on one hand, and the structures of solar coronas and solar winds on the other, is quite difficult due to such disturbances as CME that frequently occur during the solar maximum. Although CR2028 is a period of the declining phase, solar magnetic fields are moderately complex and no CME occurs during this period. For these reasons, the CR2028 period had been used for the purpose of testing the model.

3.1 Detailed structure of solar coronas

Figure 3 shows what calculated solar-internal coronas should look like. Each curve denotes a magnetic field line. Shading and contour lines represent the temperature and mass outflux in the 1.2 R_s plane. Temperature distributions in a corona are shown by magnetic field lines in different colors. The longitude centers in the coronas in panels (a) to (d) are 360, 270, 180 and 90 degrees (Carrington longitude), and associated with views of the sun from the earth on March 25, March 31, April 7, and April 14, 2005. Images taken by an extreme ultraviolet imaging telescope (EIT) camera mounted on the SOHO satellite are presented for comparison purposes. Due to the unavailability of EIT images for March 25 to 30 (360 to 330 degrees Carrington longitude), the image taken on April 21 (0 degrees Carrington longitude) is used instead of the March 25 image (360 degrees Carrington longitude).

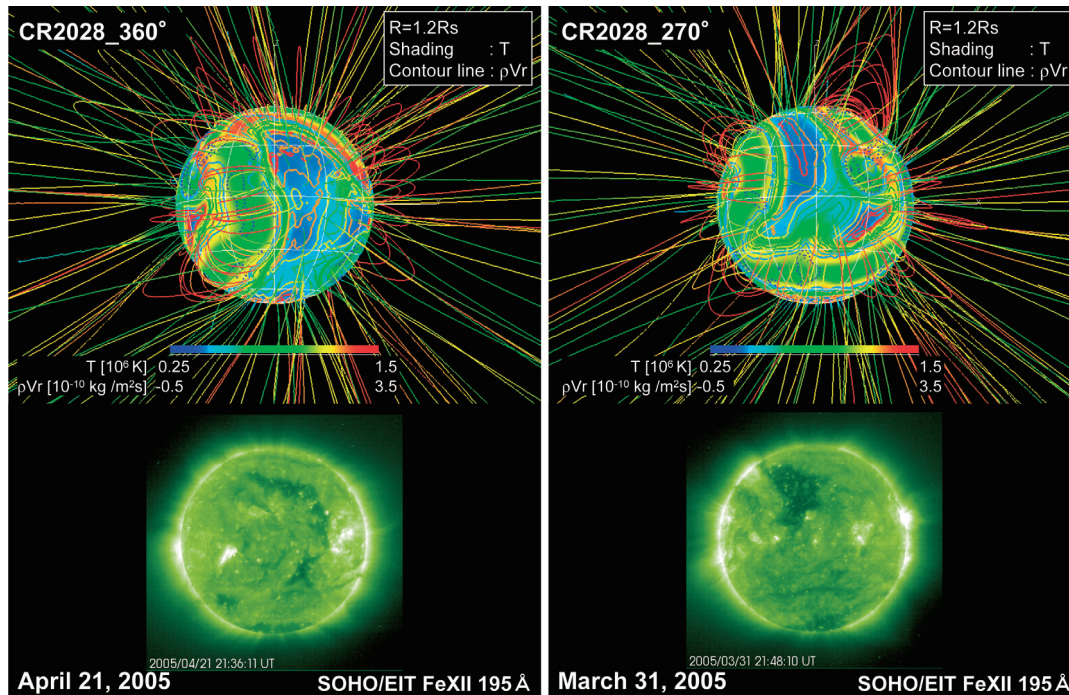


Fig.3 Simulated solar-internal coronas during CR2028

The longitude centers in panels (a) to (e) are 360, 270, 180 and 90 degrees in the Carrington coordinate system, and associated with views of the sun from the earth on March 25, March 31, April 7, and April 14, 2005. Each curve denotes a magnetic field line. Shading and contour lines represent the temperature and mass outflux in the 1.2 Rs plane. Temperature distributions in the corona are shown by magnetic field lines in different colors. Images captured on the corresponding dates by the EIT (Extreme ultraviolet Imaging Telescope) camera mounted on the *SOHO* satellite are presented in the lower parts of the panels. Due to the unavailability of EIT images for March 25 to 30 (360 to 330 degrees Carrington longitude), the image captured on April 21 (0 degrees Carrington longitude) is used instead of the March 25 image (360 degrees Carrington longitude).

Magnetic field lines are relatively hot from their base to the coronas in a closed magnetic field region, but remain cold in an open magnetic field region. These temperature structures that depend on the magnetic field configuration result from the effects of energy loading, loss, and thermal conduction in the energy equations as described in the preceding chapter.

In a closed magnetic field region, energy loading would be inadequate to allow plasma pressure overcome the Lorentz force, in which case the corona plasma would be confined by magnetic tension, with energy loading being mainly directed to heat the plasma. Because the plasma is unable to exit the confinement region, localized energies are redistributed

along the closed field lines to eventually heat the entire magnetic field. Conversely, in an open magnetic field, the plasma force exceeds the magnetic force thanks to energy loading, in which case the plasma is free to exit to interplanetary space, allowing the loaded energy to be converted more into kinetic energy than thermal energy. Even though the loaded energy is initially converted to heat the plasma, rises in localized temperature increase the pressure gradient, with its force accelerating the plasma flow. In the open magnetic field, the loaded energy is thus carried into interplanetary space along with the plasma flow, instead of being stored as thermal energy. As is evident in Fig. 3, regions with large mass outflux and low-temperature regions are dis-

tributed, overlapped, and under an open magnetic field region.

While a low-temperature region with large mass outflux under open lines of magnetic force is considered to reproduce a corona hole, such a region might be compared with EIT images obtained by SOHO. In an EIT image, a corona hole is distinguished as a dark region (with low radiation luminosity), whereas an active region is identified as a bright region (with high radiation luminosity). Simulated and observed corona holes are found in good agreement in terms of both geometry and position. For the purpose of discussions that follow, significantly conspicuous corona holes are numbered: the corona hole stretching from the South Pole to the Northern Hemisphere in the vicinity of 30 degrees Carrington longitude (middle in Fig. 3 (a) and east in Fig. 3 (e)) is designated CH1; the corona hole existing in the Northern Hemisphere in the vicinity of 270 degrees Carrington longitude (middle in Fig. 3 (b)) is designated CH2; the corona hole existing in the Northern Hemisphere in the vicinity of 150 degrees Carrington longitude (northeast in Fig. 3 (c) and at the north-west end in Fig. 3 (d)) is designated CH3.

Likewise, Fig. 4 shows a near view of the sun, offering a perspective of the correspondence between the solar disk structure and large-scale heliospheric structures. Here, the magnetic field lines are colored by polarity, with each red line designating a magnetic field line with its polarity “Away” from the sun, and each blue line designating a magnetic field line with its polarity “Toward” the sun. Contour lines represent the radial mass flux in the plane with a radius of 1.2 Rs. The longitude center is 180 degrees Carrington longitude as in Fig. 3 (c). The magnetic neutral sheet marked in orange differentiates the polarities of individual magnetic fields. Those groups of magnetic field lines that share the same polarity originate from regions on the spherical surface having the same polarity. As is evident from this figure, CH2 and CH3 share the same polarity (Toward), whereas CH2 has the opposite (Away) polarity (since it

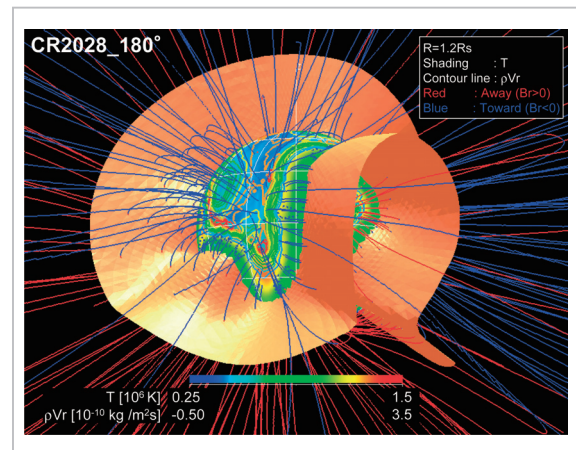


Fig.4 Perspective of correspondence between the solar disk structure and large-scale heliospheric structures

The longitude center is 180 degrees Carrington longitude as in Fig. 3 (c). Each red line designates a magnetic field line with its polarity moving “Away” from the sun; each blue line designates a magnetic field line with its polarity moving “Toward” the sun. Contour lines represent the radial mass flux in the plane having a radius of 1.2 Rs. The contour marked in orange designates a magnetic neutral sheet.

is located on the opposite side). The swelling structure of the magnetic neutral sheet caused by the magnetic field of Away polarity stretching to the Northern Hemisphere in the vicinity of 210 degrees Carrington longitude is also characteristic of this period. The differentiation of polarities and location of corona holes help establish such large-scale heliospheric structures as sector structures and the solar wind velocity distributions discussed in the next section.

3.2 Large-scale solar wind structures

Figure 5 shows the heliospheric equatorial plane as viewed from the North Pole, with the center and outer edge corresponding to the sun and a circle having a radius of 200 Rs, respectively. White lines correspond to 360, 270, 180 and 90 degrees Carrington longitude (as associated with March 25, March 31, April 7, and April 14, 2005); the red and blue markings each designate a sector polarity. As in Fig. 4, red denotes “Away” polarity and blue

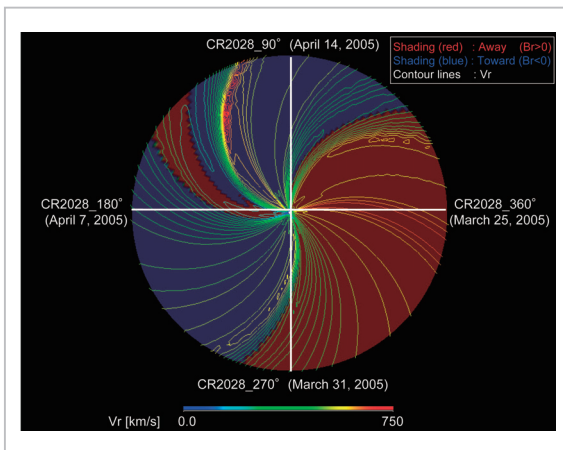


Fig.5 Large-scale solar wind structure of the heliospheric equatorial plane obtained by simulation

The center and outer edge correspond to the sun and a circle having a radius of 200 Rs, respectively. White lines correspond to 360, 270, 180 and 90 degrees Carrington longitude (as associated with March 25, March 31, April 7, and April 14, 2005); red and blue markings designate Away and Toward polarity, respectively, as in Fig. 4. Each contour line represents a radial solar wind velocity.

denotes “Toward” polarity. These polarities are superimposed with contour lines denoting a radial solar wind velocity. It can be presumed from this figure that interplanetary space during this period consists of three large sectors that involve fast solar winds, and one small sector that does not. With reference to the figure discussed in the preceding section for these sector/solar wind structures, the sectors are found to have a one-to-one correspondence with the solar disk or their sources. First, the fast solar wind in the Away sector from the first to second quadrant originates from CH1, the fast solar wind in the Toward sector expands in the third quadrant from CH2, and the last fast solar wind in the Toward sector in the fourth quadrant from CH3. The small Away sector intervening between the two large Toward sectors is associated with the swelling structure of the magnetic neutral sheet observed in the vicinity of 210 degrees Carrington longitude as shown in Fig. 4.

Next, we attempted to conduct a quantita-

tive evaluation of the simulation. To this end, we compared simulation data on the outermost edge of the calculated space with data from the ACE satellite that constantly observes solar winds at the L1 point (first Lagrangian point, one of the points of gravitational stability) as plotted in Fig. 6. The horizontal axis is time, with vertical broken lines marking the times at which CR208 started and ended. The panels from the top downward contain radial solar wind velocity V_r , plasma density N_p , plasma temperature T_p , magnetic field strength B_t , and angle ϕ formed by the magnetic field and GSE-X axis (sector polarity), with simulation data denoted by a blue line, daily averaged ACE data by a broken green line, and hourly averaged ACE data by a broken black line. Prior to the comparison process, a summary of the general pictures of observation data might be worthwhile. The period in question is characterized by three fast solar winds involving well-defined CIR on the front. One fast solar wind is found to evolve for each definite large sector at a time. The fast solar winds from the first to third sectors have Away, Toward, and Toward polarities, respectively. The sector boundary between the first and second sectors is clear, but the fast solar wind region intervening between the second and third sectors can be broken down into smaller sectors of reverse (Away) polarity. Due to the high plasma density and slow solar wind velocity, this structure may have been forged somewhat by the Away polarity field in the vicinity of the heliospheric magnetic neutral sheet stretching to the Northern Hemisphere. The simulation data and observation data were basically in good agreement. The simulation successfully reproduced not only the fast solar winds in the first to third sectors and their sector polarities, but also the small Away sectors between fast winds of Toward polarity in the second and third sectors. The simulation model may generally well reproduce the solar-heliospheric structures, despite certain drawbacks as outlined below.

Simulation data was in better agreement

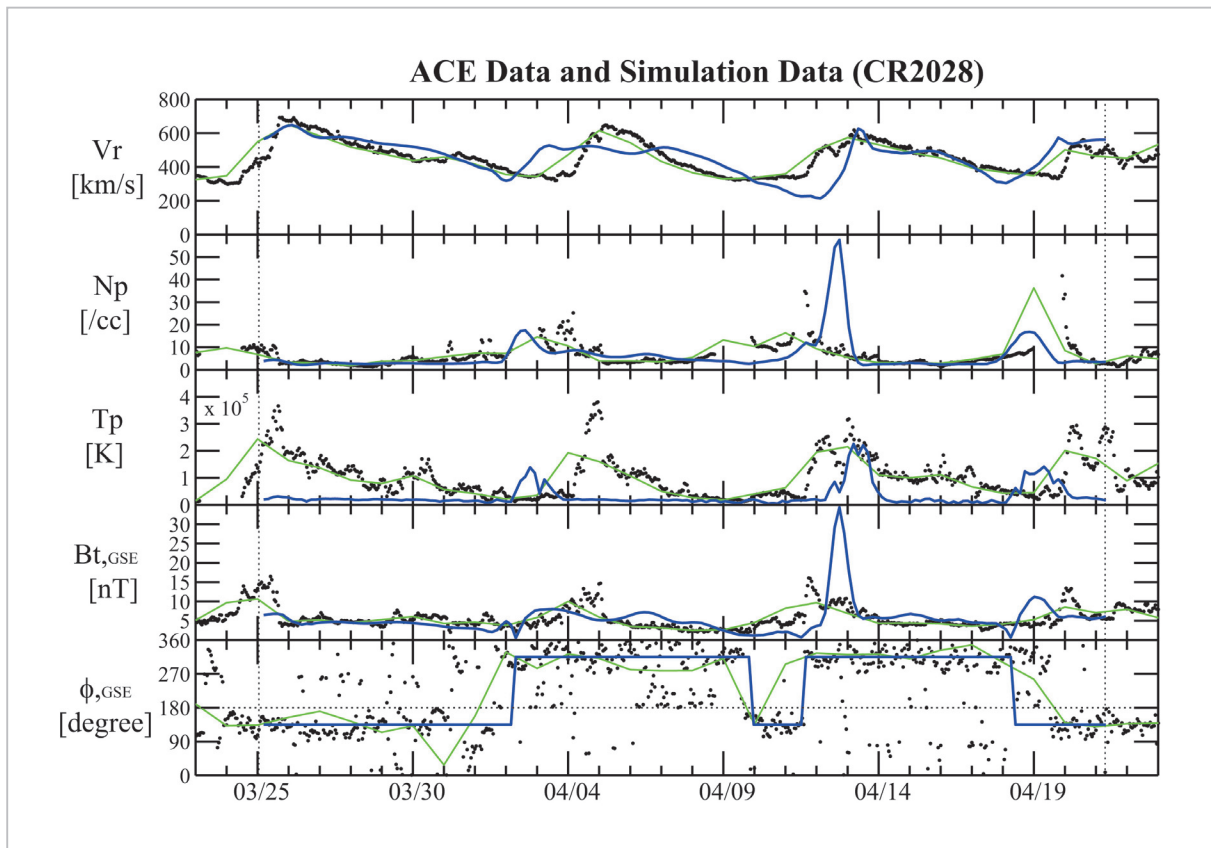


Fig.6 Comparison of simulation data with data from ACE satellite that constantly observes solar winds at L1 point (first Lagrangian point-one point of gravitational stability)

The horizontal axis is time (March 23 to April 23, 2005), with vertical broken lines marking the times at which CR208 started and ended. The panels from the top downward contain radial solar wind velocity V_r , plasma density N_p , plasma temperature T_p , magnetic field strength B_t , and angle ϕ formed by the magnetic field and GSE-X axis (sector polarity), with simulation data denoted by a blue line, daily averaged ACE data by a broken green line, and hourly averaged ACE data by a broken black line.

with the daily averaged ACE data than the hourly averaged ACE data. This relates to the spatial resolution of the present simulation. Because the MHD solution derived as a quasi-stationary structure is used as a time sequence in terrestrial orbit for the target period, spatial resolution in the longitude direction is equivalent to the time resolution of solar winds. With the period of solar rotation relative to the earth taken into account, the spatial resolution of 2.25 degrees mentioned in Section 2.1 is equivalent to a time resolution of 4.05 hours, making solar wind structures on a time scale of up to several hours unidentifiable in the current simulation. For example, increases in density, magnetic field strength, and solar wind velocity associated with the CIR clearly identified from the hourly averaged ACE data

would be smoothed in the simulation data due to the constraints on space-time resolutions, resulting in the gradient and rate of increase in wind velocity approaching the daily averaged ACE data. Even though the effect of such smoothing is taken into account, some differences still exist between the simulation data and observation data. The first difference is the arrival time of fast solar winds. The second fast wind was simulated to arrive two or three days earlier than when it actually arrived. The second difference is the absolute value of solar wind velocity. The second fast wind was simulated to have a velocity of about 120 km/s lower than the observed velocity, and the slow wind between the second and third fast winds was substantially slower than the actual velocity. Temperature changes asso-

ciated with the fast winds also exist. The temperatures during the second and third fast wind periods rose the same way as observed, but the temperature during the first fast wind period remained low. These differences may relate to both the mechanism for solar wind acceleration and the process of fast and low wind interaction. We contemplated how to overcome these difficulties by upgrading parametrization, as well as making a more precise calculation grid.

4 Discussions

Comparing the simulation results with observations as described in the preceding chapter confirmed that the model successfully reproduced both solar coronas and large-scale solar wind structures. This chapter discusses the tasks left open to future solutions, in order to make for a more accurate model.

4.1 Inner boundary conditions

Boundary conditions are necessary to conduct a simulation. For this work, we assigned magnetic observation data as an internal boundary condition, but with such plasma parameters as density and temperature being assumed uniformly distributed as in prior studies (with density fixed at $1.5 \times 10^{-13} \text{kgm}^{-3}$ and temperature at $0.5 \times 10^6 \text{K}$). Despite the generally alleged inability of MHD equations to precisely handle the microscopic processes of plasma, the finding that our model successfully reproduced solar coronas and solar winds suggests the importance of setting plasma parameters (e.g., density, temperature) to make the plasma beta (β) more likely than non-uniform plasma distributions in implementing such a solar wind simulation. This is because the MHD solution not only largely depends on β , but β also determines the effectiveness of external source terms. Therefore, let's consider the issue of the MHD solution's dependence on β . On the PFSS model, the source surface height (R_{ss}) influences the location and geometry of corona holes (where a lower R_{ss} forms a larger corona hole) [15].

Likewise on the MHD model, a higher (or lower) internal boundary β results in forming a larger (or smaller) corona hole. Assigning a smaller R_{ss} value is equivalent to overestimating the plasma force by allowing the solar magnetic field to open at a relatively low vertical height with small-scale structures relating to localized intense magnetic fields being confined to R_{ss} or below. Conversely, assigning a larger R_{ss} value is equivalent to underestimating the force of plasma. Thus, the β in MHD simulation and R_{ss} on the PFSS model exert similar effects on model output results. In considering that PSS model output is varied by the R_{ss} value, the need to carefully select the β looms into prominence. If a likely β is made selectable, practical calculations under boundary conditions based on observations like those proposed in Reference [25] would be possible.

The next section discusses the process of solar wind acceleration, though the similarity of the process of setting R_{ss} on the PFSS model to that of setting sources in an MHD simulation deserves mention. First, the boundary conditions imposed by SS mean that magnetic force is not significant above R_{ss} , and it might be logical to set R_{ss} at the Alfvén point (of 5 to 10 R_s). However, R_{ss} is actually set at a much lower vertical height (typically 2.5 R_s), thus allowing the PFSS model to provide a good reproduction of global structures. This suggests that the PFSS model accurately estimates the plasma process to some extent through the setting of R_{ss} , without describing the plasma process explicitly. Accordingly, the MHD model promises better reproducibility than the PFSS model, given the choice of a likely β and source terms. It would therefore be necessary to proceed with model development by keeping this expectation in mind.

4.2 Physical process and structures of the coronal base

It should be noted that the present model has internal boundaries located not on the precise solar surface (1.0 R_s) but in the so-called coronal base (up to 1.01 R_s) as in prior stud-

ies, in addition to assuming uniform plasma distributions on the internal boundaries for the sake of simplicity as mentioned in the foregoing section. The present model does not encompass the concept of radiation—a process vital to the balance of energy in the solar atmosphere. These problems are related. In a corona-solar wind region, radiation contributes little to the energy balance when compared with thermal conduction. In regions below the coronal base, including the chromosphere-corona transition layers, radiation has a non-negligible impact on the energy balance, so that such thermodynamic structures as density and temperature can be established from that balance. We proceeded with calculations starting with a corona that had been somewhat heated and a smoothed internal boundary, by disregarding the microstructures below the coronal base and the radiation process. Such simplification offers a good means of approximation for probing into the large-scale structure and dynamics of the corona-solar wind region. Because the present model used a normalized temperature of $0.5 \times 10^6 \text{K}$, which is much lower than that used in prior studies, it may well accommodate part of the solar wind acceleration process occurring somewhat below the coronal base. To precisely reproduce the detailed structures and dynamics of the solar atmosphere in a region of lower vertical height, however, it would be necessary to accommodate the radiation process and bottomside regions, including the chromosphere-corona transition layers. Such an attempt would also be needed in launching realistic probes into issues posed by the non-uniformity of plasma distributions, as well as the formation of short magnetic loops relevant to active regions, prominence, flares, CME, and other phenomena. The work of including a bottomside structure into a 3D global model is made extremely difficult, however, by sharp changes in the relevant plasma parameters. These are left outside the scope of our modeling for now. Such bottomside structures should be handled in precise terms in the near future to gain insight into the process of cou-

pling between the chromosphere-corona transition layers and the photosphere, as well as the coronal heating process and corona dynamics. The chromosphere model discussed in Reference [26] is the first endeavor launched in this direction, and the findings have actually resulted in a more detailed structure of regions below the coronal base.

4.3 Parameterization of solar wind acceleration

One task considered vital for modeling solar winds is how to handle coronal heating and the solar wind acceleration process. Since how to parameterize solar wind acceleration in an actual magnetic field configuration has yet to be established, how both photospheric magnetic field data and source terms can be encompassed in a self-consistent manner has loomed as a modeling task. In our work, source terms have been introduced into a system of equations for momentum and energy conservation. Although these function forms have long been used, we employed magnetic flux tube expansion factor f_s to adjust external source term strength. This concept is based on the “anti-correlation relation between f_s and solar wind velocity” that has generally been accepted since Reference [21], and is expected to produce changes in solar wind velocity by way of realistic solar corona magnetic fields. The method has been verified as being useful by running a simulation, but should call for discrete parameterization with the points described below taken into account.

It is assumed that only a heating term is available as a source term. Within a magnetic flux tube in which f_s is low, the effects of intense heating and thermal conduction maintain a high pressure gradient force, even at a high vertical height. Conversely, within a magnetic flux tube in which f_s is high, the pressure gradient force will attenuate sharply. This tendency appears favorable in producing variations in solar wind velocity that meet the “anti-correlation relation between f_s and solar wind velocity.” Yet, it should be remembered that the behavior of solar wind plasma varies

depending on where the heating energy is consumed: in a subsonic region or supersonic region. Generally, heating increases the density scale height. Because the kinetic energy per particle is inversely proportional to the density, heating in a subsonic region would reduce the asymptotic velocity of solar winds. Extreme heating dependent solely on fs might yield results totally conflicting with expectations. Effective solar wind acceleration dictates that the plasma density not be increased excessively in a subsonic region.

Momentum addition conducted here is one solution to work around the problems above, and has been found to work successfully. As explained in Section 3.2, our parameterization is not yet final. The most direct approach to upgrading the parameterization process is to implement the results of theoretical studies involving kinetics (such as [27]) in the MHD model. Most of these theoretical studies to date, however, have been directed to solar wind acceleration within a large polar corona during the solar minimum. Because our goal is to predict solar winds under all possible conditions of solar variability, a universal scheme of parameterization that accommodates various magnetic field configurations must be developed. In recent years, low-frequency MHD waves have been introduced to successfully reproduce the solar wind acceleration process on a one-dimensional MHD model as reported in Reference [28]. Because a specific scheme of parameterization for a global model is suggested from such middle-scale phenomena, MHD models that adopt three-dimensional and real solar magnetic fields must eventually employ the results of middle-scale studies. Moreover, the use of such techniques as WKB approximation has been attempted on low-dimensional models and models having solar magnetic fields simplified into dipoles [29][30].

4.4 Implementing a solar-solar wind-terrestrial integrated simulation system

Since the advent of advanced studies as reported in References [31][32], global MHD

models that calculate the terrestrial orbit (or any farther point) from solar coronas have been developed. These include solar corona inner heliosphere coupling models (see [33]) and integrated solar-terrestrial system models based on the adaptive mesh refinement (AMR) method (see [23][34][35]). Modern advances in space weather research technology have encouraged CME simulations on these models (see [35]), assuming that the background solar wind structure is similar to that observed during the solar minimum. CME, however, frequently occurs not during the solar minimum but during the solar maximum and declining phase. As pointed out in Reference [36], a precise description of the status of interaction between background solar winds and the CME forms an integral aspect of the effort to gain precise insight into the CME propagation process. Hence, modeling solar wind structures based on actual solar magnetic fields is of vital importance to exploring the CME propagation process through simulation. Our work follows this direction. We are developing a model with a view to implementing it in the NICT integrated space weather simulation system in the near future.

Calculations for this work were conducted in a fifth-order splitting grid system. As explained in Section 3.2, a spatial resolution of 2.25 degrees translates to a time resolution of about 4.05 hours in this grid system. This time scale is obviously much longer than that of various space weather phenomena. Magnetic storms, for example, may last several hours to about one day, but their growth and attenuation are controlled by solar wind variations on a time scale of several tens of minutes. The available resolution is inadequate even for reproducing solar winds/IMF variations pertaining to events having the longest time scale in the solar-terrestrial system. Moreover, as a key topic in solar-terrestrial physics, magnetospheric substorms (having a time scale from several tens of minutes to several hours) are controlled by solar wind variations having a shorter time scale. We are also pursuing the

high parallelization of MHD codes, since predicting such space weather phenomena requires computation on a higher-order splitting grid system.

5 Real-time operations

This chapter introduces a real-time implementation of the solar-solar wind MHD simulation model discussed so far. NICT is now developing integrated space weather simulation to make numeric space weather prediction possible. A real-time solar-solar wind MHD simulation model has already been operated as part of the system.

The real-time simulation uses no fifth-order splitting grid as mentioned above, but employs a fourth-order splitting grid due to the trade-off between the space-time resolutions of the simulation and the actual computing time. The simulation takes up one node (eight CPUs) consisting of a NICT supercomputer (SX-8R, manufactured by NEC) and requires days of computing time until it converges on the steady state.

In real-time implementation of a simulation using observation data as boundary conditions, the kind of observation data to use poses an issue worthy of consideration. The simulation above uses observation data (called a “synoptic map”) collected by observing the whole solar disk for 27 days, based on the sun taking about 27 days to rotate when viewed from the earth. New and old data is intermixed in a single synoptic map. Yet, observing the whole solar disk at the same time would be impossible without an observation satellite orbiting on the reverse side of the solar disk, and observation data providing snapshot-like images of the whole solar disk is theoretically unavailable. These are the reasons why a synoptic map of solar disk magnetic field observations is used as a simulation boundary condition instead.

Because solar disk magnetic field observations are conducted using visible radiation, the goal of collecting observation data on a real-time basis can hardly be achieved by ground-

based observations, since the observation conditions depend on climatic and other conditions. Satellite observation data must therefore be used. To fill this need, a synoptic map of solar disk magnetic field observation data^[37] obtained by the MDI instrument onboard the *SOHO* satellite is used as a boundary condition for the real-time solar-solar wind MHD simulation model. Because this synoptic map is updated daily, it follows that the simulation can also be run once each day, but this is not practicable because the simulation takes days of computing time as mentioned earlier. And since the large-scale structures of solar winds are considered relatively stable and do not vary in size for a period of about 27 days (during which the sun completes one rotation), real-time simulation is run by collecting the latest version of the synoptic map at each interval of the 27-day period of solar rotation.

Because the synoptic map released as a preliminary estimation is not treated in any way (including noise elimination), it is subjected to a simple noise elimination process based on the box-car method before being interpolated and otherwise manipulated to meet the simulation input format, thereby providing a data set for use as boundary conditions. Through potential field calculations using such a data set, the MHD simulation is run to proceed with computation until the solar-wind structures settle into a steady state. The simulation results are later visualized and posted on the related website (<http://www2.nict.go.jp/y/y223/simulation/realtime/enter.html>) (Fig. 7).

The real-time system is designed to automate the workflow from acquiring observation data through data processing, setting initial conditions, making potential magnetic field calculations, and MHD simulation and visualization, to posting the results without human intervention, thereby meeting the needs of numeric space weather prediction as dictated by the evolving and integrated space weather simulation system. In its present state, real-time solar-solar wind MHD simulation does not offer the calculation accuracy needed to

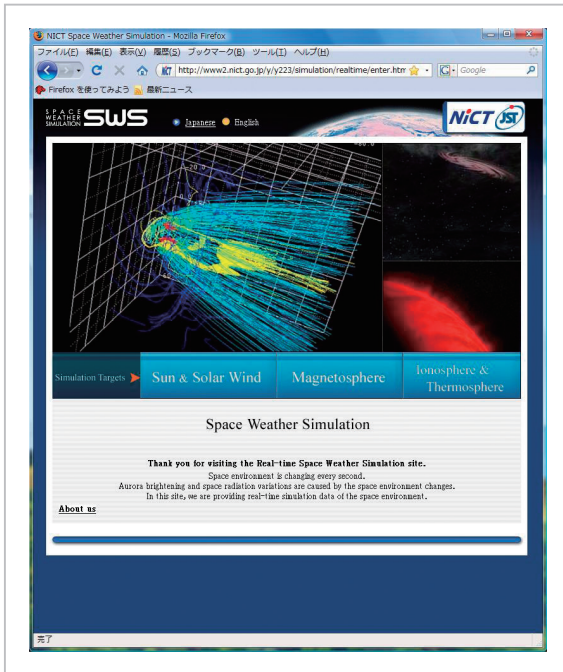


Fig.7 Real-time solar-solar wind MHD simulation website (<http://www2.nict.go.jp/y/y223/simulation/realtime/enter.html>)

satisfactorily reproduce *ACE* satellite observation data. For this reason, available solar wind data falls short of the recommended accuracy level for use as input in magnetospheric simulation. Better accuracy is therefore being sought through upgrades to the model as mentioned earlier.

6 Conclusions

A solar-solar wind MHD simulation model has been developed. A description of the system is summarized as follows:

- (1) The computational grid is formed of 2D unstructured grids stacked in the radial direction in a non-uniform manner, based on the regular dodecahedron splitting method. This grid offers the advantages of suppressing numerical instability due to the absence of singular points and simultaneously handling the detailed structure of the solar neighborhood and large-scale heliospheric structures.

- (2) Photospheric magnetic field observation data is used as an internal boundary magnetic field condition.
- (3) Momentum source, energy source and thermal conduction terms have been introduced into a system of equations to achieve supersonic solar winds. The function form of the external source term offers exponential attenuation as it has been broadly used in prior studies.
- (4) Magnetic flux tube expansion factor f_s is used to adjust the external source term strength for updating the solar wind acceleration process with an actual magnetic field configuration. The strength was weakened under large f_s and intensified under small f_s .

Simulated regions having large mass outflux on the solar surface were in good agreement with the location and geometry of corona holes presumed from SOHO/EIT images, and further simulated solar wind/interplanetary spatial parameters also corresponded well to *ACE* satellite observations, though with some differences. The present model has thus been confirmed to simultaneously reproduce the detailed structure of solar corona and the large-scale structures of solar wind successfully in a manner self-consistent with the solar magnetic field. The model is now being upgraded at NICT to determine its role in an evolving and integrated space weather simulation system.

Acknowledgements

Wilcox Solar Observatory data used in this study was obtained via the web site at <http://quake.stanford.edu/~wso> courtesy of J.T. Hoeksema. We also wish to thank the *ACE*/SWEPAM and MAG instrument teams and the *ACE* Science Center for providing the *ACE* data. The Stanford Solar Observatories Group provided the SOHO/MIDI synoptic maps (<http://soi.stanford.edu/magnetic/index5.html>).

References

- 1 Parker, E. N., "Dynamics of the interplanetary gas and magnetic fields," *Astrophys. J.*, Vol. 128, p. 664, 1958.
- 2 Alazraki, G. and P. Couturier, "Solar wind acceleration caused by gradient of Alfvén wave pressure," *Astron. Astrophys.*, Vol. 13, p. 380, 1971.
- 3 Belcher, J. W., "Alfvénic wave pressures and solar wind," *Astrophys. J.*, Vol. 168, p. 509, 1971.
- 4 Barnes, A., "Acceleration of the solar wind," *Rev. Geophys.*, Vol. 30, p. 43, 1992.
- 5 Barnes, A., P. R. Gazis, and J. L. Phillips, "Constraints on solar wind acceleration mechanisms from Ulysses plasma observations- the first polar pass," *Geophys. Res. Lett.*, Vol. 22, p. 3309, 1995.
- 6 Hollweg, J. V. and P. A. Isenberg, "Generation of the fast solar wind: A review with emphasis on the resonant cyclotron interaction," *J. Geophys. Res.*, Vol. 107(A7), p. 1147, doi: 10.1029/2001JA000270, 2002.
- 7 Cranmer, S. R., "Coronal holes and the high-speed solar wind," *Space Sci. Rev.*, Vol. 101, p. 229, 2002.
- 8 Ness, N. F. and J. M. Wilcox, "Sector Structure of Quiet Interplanetary Magnetic Field," *Science*, Vol. 148, p. 1592, 1965.
- 9 Phillips, J. L., S. J. Bame, A. Barnes, B. L. Barraclough, W. C. Feldman, B. E. Goldstein, J. T. Gosling, G. W. Hoogeveen, D. J. McComas, M. Neugebauer, and S. T. "Suess, Ulysses solar wind plasma observations from pole to pole," *Geophys. Res. Lett.*, Vol. 22, p. 3301, 1995.
- 10 McComas, D. J., S. J. Bame, B. L. Barraclough, W. C. Feldman, H. O. Funsten, J. T. Gosling, P. Riley, R. Skoug, A. Balogh, R. Forsyth, B. E. Goldstein, and M. Neugebauer, "Ulysses' return to the slow solar wind," *Geophys. Res. Lett.*, Vol. 25, p. 1, 1998.
- 11 Schatten, K. H., J. M. Wilcox, and N. F. Ness, "A model of interplanetary and coronal magnetic fields," *Sol. Phys.*, Vol. 6, p. 442, 1969.
- 12 Altschuler, M. D. and G. Newkirk, "Magnetic fields and structure of solar corona I. Methods of calculating coronal fields," *Sol. Phys.*, Vol. 9, p. 131, 1969.
- 13 Wang, Y. M. and N. R. Sheeley, "Solar wind speed and coronal flux-tube expansion," *Astrophys. J.*, Vol. 355, p. 726, 1990.
- 14 Neugebauer, M., R. J. Forsyth, A. B. Galvin, K. L. Harvey, J. T. Hoeksema, A. J. Lazarus, R. P. Lepping, J. A. Linker, Z. Mikić, J. T. Steinberg, R. von Steiger, Y. M. Wang, and R. F. Wimmer-Schweingruber, "Spatial structure of the solar wind and comparisons with solar data and models," *J. Geophys. Res.*, Vol. 103(A7), p. 14587, 1998.
- 15 Linker, J. A., Z. Mikić, D. A. Biesecker, R. J. Forsyth, S. E. Gibson, A. J. Lazarus, A. Lecinski, P. Riley, A. Szabo, and B. J. Thompson, "Magnetohydrodynamic modeling of the solar corona during Whole Sun Month," *J. Geophys. Res.*, Vol. 104(A5), p. 9809, 1999.
- 16 Zhao, X. P. and J. T. Hoeksema, "Prediction of the interplanetary magnetic field strength," *J. Geophys. Res.*, Vol. 100(A1), p. 19, 1995.
- 17 Arge, C. and V. Pizzo, "Improvement in the prediction of solar wind conditions using near-real time solar magnetic field updates," *J. Geophys. Res.*, Vol. 105 (A5), p. 10465, 2000.
- 18 Tanaka, T., "Finite volume TVD scheme on an unstructured grid system for three-dimensional MHD simulation of inhomogeneous systems including strong background potential fields," *J. Comput. Phys.*, Vol. 111, p. 381, 1994.
- 19 Brio, M. and C. C. Wu, "An upwind differencing scheme for the equations of ideal magnetohydrodynamics," *J. Comput. Phys.*, Vol. 75, p. 400, 1988.

-
- 20 Hartle, R. E. and A. Barnes, "Nonthermal heating in 2-fluid solar wind model," *Journal of Geophys. Res.*, Vol. 75, p. 6915, 1970.
 - 21 Suess, S. T., A. H. Wang, and S. T. Wu, "Volumetric heating in coronal streamers," *J. Geophys. Res.*, Vol. 101(A9), p. 19957, 1996.
 - 22 Wang, A. H., S. T. Wu, S. T. Suess, and G. Poletto, "Global model of the corona with heat and momentum addition," *J. Geophys. Res.*, Vol. 103 (A2), p. 1913, 1998.
 - 23 Groth, C., D. De Zeeuw, T. Gombosi, and K. Powell, "Global three-dimensional MHD simulation of a space weather event: CME formation, interplanetary propagation, and interaction with the magnetosphere," *J. Geophys. Res.*, Vol. 105 (A11), p. 25053, 2000.
 - 24 Levine, R. H., M. D. Altschuler, and J. W. Harvey, "Solar sources of interplanetary magnetic field and solar wind," *J. Geophys. Res.*, Vol. 82, p. 1061, 1977.
 - 25 Hayashi, K., "Magnetohydrodynamic simulations of the solar corona and solar wind using a boundary treatment to limit solar wind mass flux," *Astrophys. J. Suppl. Ser.*, Vol. 161, p. 480, 2005.
 - 26 Lionello, R., J. A. Linker, and Z. Mikić, "Including the transition region in models of the large-scale solar corona," *Astrophys. J.*, Vol. 546, p. 542, 2001.
 - 27 Withbroe, G. L., "The temperature structure, mass, and energy-flow in the corona and inner solar wind," *Astrophys. J.*, Vol. 325, p. 442, 1988.
 - 28 Suzuki, T. K. and S. Inutsuka, "Making the corona and the fast solar wind: A self-consistent simulation for the low-frequency Alfvén waves from the photosphere to 0.3 AU," *Astrophys. J.*, Vol. 632, L49, 2005.
 - 29 Usmanov, A. V., M. L. Goldstein, B. P. Besser, and J. M. Fritzer, "A global MHD solar wind model with WKB Alfvén waves: Comparison with Ulysses data," *J. Geophys. Res.*, Vol. 105 (A6), p. 12675, 2000.
 - 30 Usmanov, A. V. and M. L. Goldstein, "A tilted-dipole MHD model of the solar corona and solar wind," *J. Geophys. Res.*, Vol. 108 (A9), p. 1354, doi: 10.1029/2002JA009777, 2003.
 - 31 Usmanov, A. V., "Interplanetary magnetic field structure and solar wind parameters as inferred from solar magnetic field observations and by using a numerical 2-D MHD model," *Sol. Phys.*, Vol. 143, p. 345, 1993a.
 - 32 Usmanov, A. V., "The global structure of the solar wind in June 1991," *Sol. Phys.*, Vol. 148, p. 371, 1993b.
 - 33 Odstrčil, D., V. J. Pizzo, J. A. Linker, P. Riley, R. Lionello, and Z. Mikić, "Initial coupling of coronal and heliospheric numerical magnetohydrodynamic codes," *J. Atmos. Sol.-Terr. Phys.*, Vol. 66, p. 1311, 2004.
 - 34 Gombosi, T. I., D. L. DeZeeuw, C. P. T. Groth, K. G. Powell, and Q. F. Stout, "Multiscale MHD simulation of a coronal mass ejection and its interaction with the magnetosphere-ionosphere system," *J. Atmos. Sol.-Terr. Phys.*, Vol. 62, p. 1515, 2000.
 - 35 Tóth, G., I. V. Sokolov, T. I. Gombosi, D. R. Chesney, C. R. Clauer, D. L. De Zeeuw, K. C. Hansen, K. J. Kane, W. B. Manchester, R. C. Oehmke, K. G. Powell, A. J. Ridley, Roussev, II, Q. F. Stout, O. Volberg, R. A. Wolf, S. Sazykin, A. Chan, B. Yu, and J. Kota, "Space Weather Modeling Framework: A new tool for the space science community," *J. Geophys. Res.*, Vol. 110, A12226, doi: 10.1029/2005JA011126, 2005.
 - 36 Usmanov, A. V. and M. Dryer, "A global 3-D simulation of interplanetary dynamics in June 1991," *Sol. Phys.*, Vol. 159, p. 347, 1995.
 - 37 Scherrer, P. H., Bogart, R. S., Bush, R. I., et al., *Sol. Phys.*, Vol. 162, p. 129, 1995.



NAKAMIZO Aoi, Ph.D.

*Guest Researcher, Space Environment
Group, Applied Electromagnetic
Research Center (Faculty of Sciences,
Kyushu University)*

Solar-Terrestrial Physics Physis



KUBO Yûki

*Senior Researcher, Space Environment
Group, Applied Electromagnetic
Research Center*

Solar Particle Physics



TANAKA Takashi, Dr. Sci.

*Professor, Graduated School of
Sciences, Kyushu University*

*Magnetospheric Compound System
Physics*